

Old Dominion University ODU Digital Commons

Electrical & Computer Engineering Faculty
Publications

Electrical & Computer Engineering


2006

Melting and Solidification Study of As-Deposited and Recrystallized Bi Thin Films

M. K. Zayed
Old Dominion University

H. E. Elsayed-Ali
Old Dominion University, helsayed@odu.edu

Follow this and additional works at: https://digitalcommons.odu.edu/ece_fac_pubs

 Part of the [Atomic, Molecular and Optical Physics Commons](#), [Electrical and Computer Engineering Commons](#), [Mathematics Commons](#), and the [Semiconductor and Optical Materials Commons](#)

Repository Citation

Zayed, M. K. and Elsayed-Ali, H. E., "Melting and Solidification Study of As-Deposited and Recrystallized Bi Thin Films" (2006). *Electrical & Computer Engineering Faculty Publications*. 106.
https://digitalcommons.odu.edu/ece_fac_pubs/106

Original Publication Citation

Zayed, M. K., & Elsayed-Ali, H. E. (2006). Melting and solidification study of as-deposited and recrystallized Bi thin films. *Journal of Applied Physics*, 99(12), 123516. doi:10.1063/1.2208551

This Article is brought to you for free and open access by the Electrical & Computer Engineering at ODU Digital Commons. It has been accepted for inclusion in Electrical & Computer Engineering Faculty Publications by an authorized administrator of ODU Digital Commons. For more information, please contact digitalcommons@odu.edu.

Melting and solidification study of as-deposited and recrystallized Bi thin films

M. K. Zayed and H. E. Elsayed-Ali^{a)}

Physical Electronics Research Institute, Department of Electrical and Computer Engineering, Old Dominion University, Norfolk, Virginia 23529

(Received 7 December 2005; accepted 12 April 2006; published online 27 June 2006)

Melting and solidification of as-deposited and recrystallized Bi crystallites, deposited on highly oriented 002-graphite at 423 K, were studied using reflection high-energy electron diffraction (RHEED). Films with mean thickness between 1.5 and 33 ML (monolayers) were studied. *Ex situ* atomic force microscopy was used to study the morphology and the size distribution of the formed nanocrystals. The as-deposited films grew in the form of three-dimensional crystallites with different shapes and sizes, while those recrystallized from the melt were formed in nearly similar shapes but different sizes. The change in the RHEED pattern with temperature was used to probe the melting and solidification of the crystallites. Melting started at temperatures below the bulk melting point of Bi, $T_0=544.5$ K, and extended over a temperature range that depended on the size distribution of the crystallites. The as-deposited 1.5 ML film started to melt at T_0-50 K and melted completely at T_0-20 K. For films with higher coverage, the size distribution was observed to spread over a wider range with a larger mean value, resulting in a shift in the melting temperature range towards higher temperatures. Due to the shift in size distribution to higher values upon recrystallization, the recrystallized Bi crystallites showed a melting temperature range higher than that of the as-deposited crystallites. For the investigated conditions, all films were completely melted below or at T_0 of Bi. The characteristic film melting point, defined as the temperature at which the film melting rate with temperature is the fastest, showed a linear dependence on the reciprocal of the average crystallite radius, consistent with theoretical models. Of these models, the surface-phonon instability model best fits the obtained results. During solidification, the Bi films showed high amount of supercooling relative to T_0 of Bi. The amount of liquid supercooling was found to decrease linearly with the reciprocal of the average crystallite size. © 2006 American Institute of Physics. [DOI: 10.1063/1.2208551]

I. INTRODUCTION

The solid-liquid phase transition of nanoscale systems has been extensively studied for the purpose of gaining an atomistic understanding of the phase transition properties and how it is affected by the reduced size.¹⁻⁶ Nanocrystals have melting and solidification behaviors that are different from their own bulk materials. An abrupt change in the physical properties upon melting characteristic of first-order phase transition is observed for bulk crystals, whereas that of nanocrystals spreads over a temperature range and has strong size dependence.¹⁻¹⁰ Also, the role of surface and interfacial energies becomes crucial.^{2,11-15} While the reduced size is known to cause melting point depression, the effect of the surface and interfacial energies can lead to either melting point depression or superheating for certain crystal morphologies.¹⁻¹⁵ nanocrystals embedded in a host matrix have melting and solidification behaviors that are mainly controlled by the interfacial energy,¹¹⁻¹⁵ while those grown on relatively inert substrates give information on the thermodynamic nature of the transition with minimal interface effects.^{2,4,7,8}

Bi has an anisotropic crystal structure, low bulk melting

point T_0 , low partial vapor pressure near T_0 , and undergoes negative volume change upon melting.^{7,16,17} These properties have stimulated numerous experimental and theoretical studies to better understand its solid-liquid phase transition.¹⁸⁻²¹ While a size-dependent melting point depression consistent with theoretical models is commonly observed,^{12,20,21} a subset of the formed crystallites was previously observed to superheat above T_0 .^{7,18,19} Furthermore, experimental and theoretical studies have shown that superheating of the solid phase is possible for many materials that undergo positive volume change upon melting.²²⁻²⁵ Thus, it is believed that the solid-liquid interfacial energy and/or crystal shape, rather than the volume change upon melting, is the reason for the observed superheating.^{16,18}

Because of the surface energy anisotropy, crystals bounded by different orientations melt at different temperatures. For nanocrystals, the anisotropy in surface energy affects their external shapes as well as their melting behaviors.^{26,27} Crystallites recrystallized from melt can have shapes and external surface morphologies that differ from those as-deposited, therefore, the melting and solidification behaviors can differ between the two types. Atomic force microscopy (AFM) showed that as-deposited indium films deposited on a graphite substrate at room temperature form shallow nanocrystals with different shapes, while recrystal-

^{a)}Author to whom correspondence should be addressed; electronic mail: helsayed@odu.edu

lized nanocrystals were formed in more rounded polyhedral shapes.²⁸ Melting and solidification studies of these nanocrystals using reflection high-energy electron diffraction (RHEED) showed that the shape as well as the size of the formed nanocrystals affect their melting behavior.²⁸ Indium films composed of high density of nanocrystals with minimum energy facets were found to melt at higher melting point than those with lower densities but larger average sizes.²⁸ Both films were melted completely at temperatures below the bulk melting point of In. Dark field electron microscopy was used to investigate the melting of Bi crystallites in as-deposited and recrystallized Bi films on a carbon substrate.¹⁸ As-deposited films were found to have crystallites that are different in shape and in melting behavior from those recrystallized after melting. While a subset of the as-deposited crystallites, with elongated platelet shape, superheated by 7 K above T_0 , the recrystallized polyhedral hexagonal shaped crystallites in the as-deposited film showed melting point depression.¹⁸ Using the same technique to study the melting of lead crystallites, superheating by 2 K was found for extensively {111} faceted platelet-shaped crystallites formed in the as-deposited films.²³ Lead crystallites with other shapes melted below T_0 . By recrystallizing a 1000 Å average thickness lead film previously deposited on a graphite substrate at room temperature, Mètois and Heyraud were able to prepare some crystallites bounded by minimum energy facets with sharp edges that were superheated by ~ 3 K.²²

RHEED is a surface sensitive technique capable of probing the structural integrity of crystalline solids within a penetration thickness given by the inelastic mean free path (IMFP) of the electrons. The low electron current and the grazing angle geometry of RHEED allow for probing a wide surface area with negligible electron heating effects. Recently, we have used *in situ* RHEED and *ex situ* AFM to study the effect of deposition temperature on the structure and morphology of thermally deposited Bi on graphite.²⁹ We found that films deposited around 415 ± 5 K formed rounded polyhedral as well as elongated platelet Bi nanocrystals. Bi crystallites having similar elongated platelet shape previously showed ~ 7 K superheating.¹⁸ In this work, melting and solidification of Bi crystallites in as-deposited and recrystallized films were studied using RHEED. *Ex situ* AFM is used to study the morphology and size distribution of the deposited films. As-deposited Bi films were found to form three-dimensional (3D) crystallites with different shapes and sizes, while those recrystallized from the melt were found to form crystallites with nearly similar shapes but different sizes. The effect of the crystal shape and size on the melting behavior of the crystallites is discussed.

II. EXPERIMENTAL METHOD

Bi films were prepared and investigated in an ultrahigh vacuum (UHV) chamber ($\sim 5.0 \times 10^{-10}$ Torr base pressure) equipped with RHEED. The chamber's base pressure remained almost constant during melting and solidification experiments, while a small increase in pressure was observed during deposition. Highly oriented pyrolytic 002-graphite

(HOPG) was used as a substrate. HOPG is chemically inert. The deposited Bi interacts with the graphite substrate via the van der Waals attraction force with no interdiffusion or chemical compound formation. The graphite substrate is loaded in the UHV chamber immediately after cleaving it in air. The substrate is mounted on a resistively heated stage capable of reaching temperatures up to 1000 K. Before deposition, the graphite substrate is heated to ~ 770 K for 10 min in order to evaporate any adsorbed gases and obtain a clear graphite RHEED pattern. A K-type thermocouple, placed in contact with the surface of the substrate, was used to measure the surface temperature of the substrate and the deposited film. The thermocouple was calibrated in air to the bulk melting point of pure Bi. This calibration is performed before and after the experiment in order to assure that the properties of the thermocouple were not altered during the heating and cooling cycles. A temperature measurement uncertainty of ± 1 K was obtained.

Bi with 99.999% purity was evaporated from a resistively heated tungsten basket. The substrate temperature was kept at 423 K for ~ 10 min before deposition. RHEED was used to monitor the deposition and the growth of the deposited films. The film coverage was obtained using a calibrated quartz crystal thickness monitor. By controlling the current applied to the heater filament, the deposition rate was maintained between 0.4 and 0.7 Å s⁻¹. Bi has an average Bi–Bi bond length of 3.24 Å, which is used to express the measured film thickness in monolayer (ML). Films with different coverage, from 1.5 to 33 ML, were prepared. The as-deposited samples were investigated immediately after cooling to room temperature. The recrystallized samples were heated a few degrees above T_0 and maintained at that temperature for a few minutes, then slowly cooled to room temperature. The reappearance of the Bi diffraction pattern during cooling indicates its recrystallization.

RHEED diffraction patterns were obtained using a 9.7 kV electron beam. A computer-controlled charge coupled device (CCD) camera was used to record the diffraction patterns that were displayed on a phosphorous screen. The heating and cooling rates were kept almost constant between 3 and 4 K min⁻¹ by controlling the current of the heating stage. These heating rates were in the range of previous melting and solidification experiments in which Bi crystallites showed a time-dependent melting behavior and a subset of these crystallites superheated by ~ 7 K.¹⁸ The RHEED patterns were recorded during heating and cooling. Each RHEED pattern was acquired in ~ 0.17 s, thus, temperature changes during pattern acquisition were negligible. Bi has a relatively low bulk melting point ($T_0 = 544.5$ K), which facilitates the melting experiment. The low Bi vapor pressure near T_0 [$< 2 \times 10^{-10}$ Torr (Ref. 17)] allows for conducting the melting experiment with negligible atom loss by evaporation. Bi films were easily reevaporated off the substrate at the end of the investigation by holding the substrate at 970 K for a few minutes. A clear graphite pattern was observed, which indicated complete evaporation of the deposited Bi off the graphite. Thus, melting and solidification of different film thicknesses can be performed on the same substrate.

For film morphology studies, films with different cover-

age were prepared in the UHV chamber. After completion of the film deposition and any heat treatment, the chamber was vented to atmospheric pressure using argon gas and the films were taken out. *Ex situ* AFM operated in a tapping mode in air at room temperature was used to study the morphology and size distribution of the nanocrystals. The lateral and height resolutions of the AFM used is 1 and <0.1 nm, respectively, as specified by the manufacturer.

III. RESULTS AND DISCUSSION

A. Film deposition and characterization

The films studied were prepared at a substrate temperature of 423 K. RHEED observations during deposition of Bi films on the HOPG substrate showed a continuous decay in the normalized intensity of the (002) graphite spot. Within the deposited thickness range, no spots related to Bi were observed during deposition. However, clear transmissionlike RHEED patterns of Bi were observed as the films were cooled to room temperature. A detailed RHEED study of Bi deposition on (002) graphite revealed that films deposited at temperatures higher than 415 ± 5 K were condensed in a quasi-liquid supercooling state. When these films were cooled below the maximum supercooling point of Bi, ~ 398 K, they solidified into the rhombohedral structure of Bi with morphologies that were determined by the initial supercooling point from which the film crystallized.²⁹

After cooling to room temperature, as-deposited and recrystallized Bi films showed transmission diffraction patterns consisting of spots aligned along rods normal to the surface. The patterns were indexed based on the 3D reciprocal lattice mesh of the rhombohedral structure of Bi. The RHEED pattern of as-deposited 1.5 ML Bi films and its corresponding indexing is shown in Fig. 1(a). As-deposited films with coverage of 1.5–10 ML showed similar patterns. The pattern is composed of superposition of two spot sets representing two different diffraction zones, $\langle 1\bar{1}\bar{1} \rangle$ and $\langle 00\bar{1} \rangle$, that have the (110) as a common orientation parallel to the substrate surface. This indicates that Bi grows on the HOPG surface as ensembles of 3D crystallites with their (110) surfaces parallel to the (002) of the graphite. The presence of two diffraction zones indicates that the crystallites have different lateral orientations on the basal graphite plane, or have misalignment angle $\sim 40^\circ$ relative to each other, which is the angle between the observed zone directions. Formation of nanocrystals with two or more lateral orientations, due to substrate effects, has been previously reported.^{30,31} Using AFM, we observed elongated Bi crystallites that are influenced by the crystal symmetry of the substrate in spite of the weak interaction. Also, some spots corresponding to the graphite surface (pointed at by arrows in Fig. 1) were still observable even at higher film coverage. This is indicative of the low surface coverage of the formed Bi crystallites. As the Bi coverage was increased to 15 and 33 ML, Fig. 1(b), the misalignment and randomness of the grown crystallites in the as-deposited films increased. This results in diffraction patterns that are characteristic of textured films.³² No change in the relative spot positions was observed as the film thick-

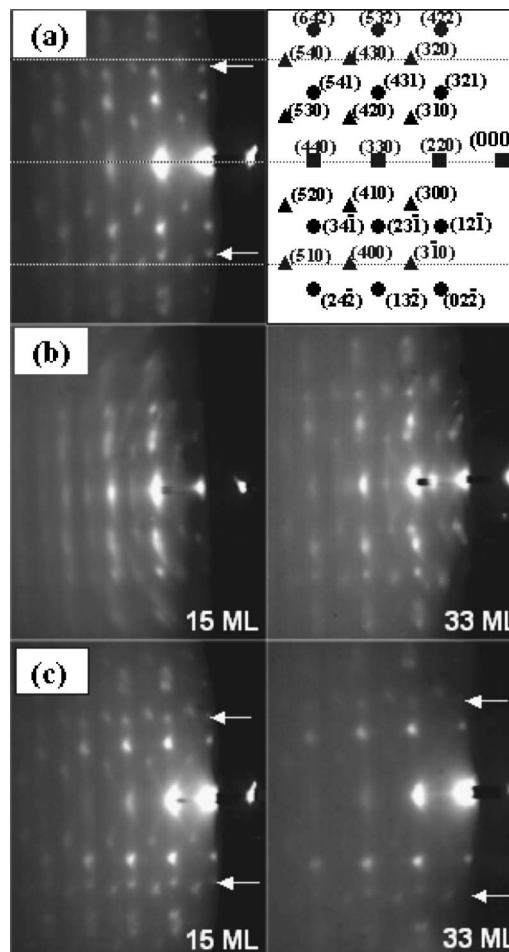


FIG. 1. (a) RHEED pattern of as-deposited 1.5 ML Bi film and its corresponding 3D indexing (●: spots of $\langle 1\bar{1}\bar{1} \rangle$ diffraction zone, ▲: spots of $\langle 00\bar{1} \rangle$ diffraction zone, and ■: spots of the common 110 orientation). RHEED patterns of (b) as-deposited and (c) recrystallized Bi films of 15 and 33 ML mean thicknesses. The films were deposited at 423 K and the patterns were taken after cooling to room temperature for both as-deposited and recrystallized films. The arrows point at graphite spots that are still observable even at large film thickness due to incomplete surface coverage.

ness was increased. This indicates that no structural and/or orientational change with the thickness occurred.

For 1.5–10 ML films, no noticeable change in the RHEED pattern was observed between as-deposited and recrystallized films. However, the RHEED patterns of the 15 and 33 ML Bi films changed after recrystallization from that of textured films to patterns of films that have two orientation crystal sets, Fig. 1(c). Moreover, the $\langle 1\bar{1}\bar{1} \rangle$ diffraction zone in the recrystallized films prevailed and the diffraction spots of the $\langle 00\bar{1} \rangle$ zone were barely seen for the 33 ML film. Such pattern suggests that the crystallites are preferably oriented along the $[1\bar{1}\bar{1}]$ direction. Another consideration is that the RHEED penetration depth and shadowing effects could affect the diffraction pattern.³³ RHEED probes a shell given by the IMFP of the electron beam within the probed nanocrystals, which is ~ 9 nm for 9.7 kV electron beam into Bi as calculated from the general equation of IMFP.³⁴ Within this probed depth, the RHEED pattern is a result of diffractions from all crystallites forming the film in the few mm^2 probed area. The shadowing effect is expected to increase with in-

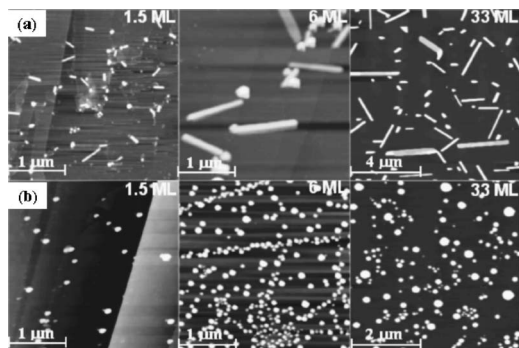


FIG. 2. AFM images of (a) as-deposited and (b) recrystallized Bi films with different coverage. Elongated nanocrystal aligned in the directions of minimum lattice misfit and angular distortions are observed in the as-deposited films. Recrystallized films are formed in more rounded polyhedral similar shapes.

creasing film thickness because of the anisotropic crystal growth that results in height differences between the crystallites forming the film. The effect of shadowing is limited at the lower coverage ratios. Thus, the dominance of one diffraction zone over the other is mainly due to film orientation enhancement.

Postdeposition AFM was used to study the morphology of as-deposited and recrystallized Bi films, as shown in Fig. 2. As-deposited Bi films were found to form 3D crystallites with different shapes and sizes, while those recrystallized from melt were found to form 3D crystallites with nearly the same shape but different sizes. Crystallites with different shapes including rounded, polyhedral, elongated platelet, and triangular shapes are observed in as-deposited films. For the recrystallized films, faceted polyhedral-shaped crystallites mostly with curved edges, but in some cases with sharp edges, were observed. Formation of crystal facets is due to the anisotropic surface energy and the surface free energy temperature and size dependences.^{27,28,35} Rounded or curved surfaces indicate the presence of all surface orientations in the formed nanocrystals, however, sharp-edged shapes indicate missing orientations in the formed crystallites.³⁵ As reported previously, the curved regions increase in size with temperature, at the expense of the plain facets, due to the decrease in surface energy anisotropy until a spherical shape is formed as the nanocrystal is completely melted.^{27,28} Annealing near T_0 or cooling from the melt allows all possible surface orientations to appear in the final form of the nanocrystals.

The crystallites were uniformly distributed throughout the substrate surface except at terrace edges where a higher density of crystallites was found. Among all possible nucleation centers, terrace edges offer minimum energy barrier for nucleation. The crystallites that nucleated at terrace edges grew outward as observed in Fig. 2. Thus, the density of the formed crystallites was influenced by the density of substrate terrace edges, which is random due to cleavage. The majority of the elongated crystallites were found to be aligned either parallel to each other, with $\sim 5^\circ$ misalignment, or intercepting at angles of either 60° or 120° . Few crystallites were found intercepting at angles of 30° and 90° . This growth directionality suggests that the growth of Bi is influenced by

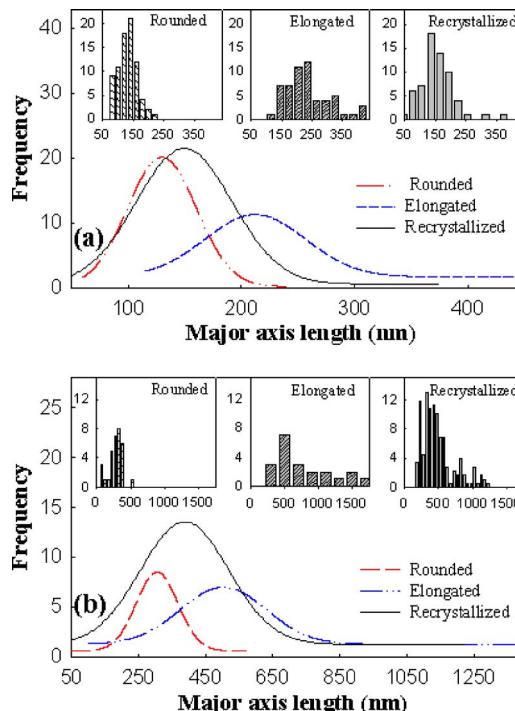


FIG. 3. Size-distribution histograms and the corresponding Gaussian function fits for as-deposited and recrystallized Bi film of (a) 1.5 and (b) 33 ML coverage. Two histograms accounting for the elongated and rounded Bi crystallites are generated for as-deposited films, while one histogram is generated for recrystallized films.

the graphite structure in an epitaxial-like growth mode, in spite of the weak interaction with the substrate. In this case the overlayer has a lattice spacing different from that of the substrate, but grows with an orientation that is affected by the substrate. A similar observation was reported for the growth of Bi on III-V(110) substrates.³⁶ It is the weak interaction between these substrates and Bi and the use of very low deposition temperature, 30 K, that enabled such epitaxial directional growth in spite of the presence of a large lattice mismatch, $\sim 20\%$.³⁶ For a graphite substrate, Bi adatoms were reported to be highly mobile on its basal plane and the growth was site limited rather than diffusion limited.³⁷ Because of the inertness and weak interaction of graphite with Bi, in addition to unrestricted adatom diffusion, Bi grows favorably in directions of minimum mismatch with the graphite substrate. Based on the structure symmetry of Bi and 002-graphite plane, these epitaxial relations were found to be either with $[110]_{\text{Bi}} \parallel [120]_{\text{graphite}}$ or $[010]_{\text{Bi}} \parallel [010]_{\text{graphite}}$, where minimum lattice misfit and angular distortion exist.³⁷

In order to study the size distribution of the Bi crystallites of the deposited films, the major and minor axes of the formed crystallites were measured from images similar to those of Fig. 2. Histograms representing the size distribution of as-deposited and recrystallized crystallites were generated. Accounting for the different crystal shapes, two distributions were generated for as-deposited films: one for elongated and the other for rounded polyhedrons. For recrystallized films, only one distribution is generated. Figure 3 shows the size distributions of as-deposited and recrystallized Bi crystallites for films of 1.5 and 33 ML average thicknesses. A Gaussian function fit of the distributions is plotted on one graph for

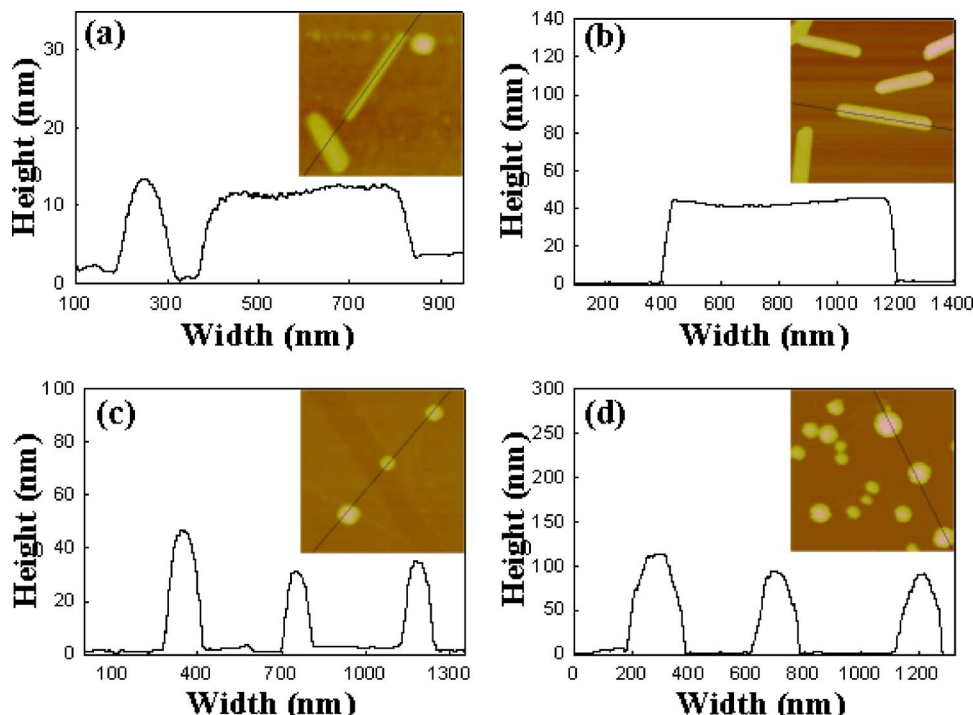


FIG. 4. AFM line profile analysis along some crystallites of Bi films with different coverage: (a) as-deposited 1.5 ML, (b) as-deposited 33 ML, (c) recrystallized 1.5 ML, and (d) recrystallized 33 ML crystallites.

comparison. Analysis of images, taken at different locations on the surface, showed that the size distribution is sensitive to the location selection for low thicknesses, 1.5–10 ML, while insignificant dependence on location was found for films with large thicknesses. The random nature of substrate terrace density upon cleavage contributes to this location dependence of the nanocrystal size distribution. Similar observation was reported previously in the deposition of metallic crystallites on a cleaved graphite substrate.²⁸ Crystallites that are away from terrace edges are normally larger in size. The distributions became wider and shifted toward higher values as the coverage increased from 1.5 to 33 ML. For recrystallized rounded crystals, the full width at half maximum (FWHM) of the distributions increased from ~ 102 to ~ 333 nm and the most probable value increased from ~ 150 to ~ 388 nm as the thickness increased from 1.5 to 33 ML. Similar behavior was observed for as-deposited films, where both elongated and rounded distributions are widened and shifted to higher values. Due to shape deformation upon recrystallization, rounded crystallites were found to have larger average heights than as-deposited elongated crystals. Figure 4 shows line scan analysis across some as-deposited and recrystallized Bi crystals for films of 1.5 and 33 ML average thickness. For 1.5 ML film the height increased from ~ 10 to ~ 20 nm, while for 33 ML it increased from ~ 40 to > 80 nm as the films were recrystallized after melting.

B. Melting of Bi films

Melting and solidification of as-deposited and recrystallized Bi films were studied by monitoring the intensity of the Bi (220) spot as a function of temperature. The intensity is normalized to its value at or near room temperature. Figure 5 shows the natural log of the normalized intensity as a function of temperature during heating and cooling of as-

deposited films with different coverage. Similar curves were obtained for recrystallized films. With heating, the measured RHEED spot intensities decreased due to thermal effects according to the Debye-Waller factor. At some temperature, a sharper intensity decrease occurred due to a decrease in the long-range order of the probed nanocrystals. The decrease in the RHEED intensity due to film partial melting is gradual and spans over a temperature range, whose onset and end points increase with film thickness. As the film melted completely, the RHEED intensity decreased to its minimum value and only the inelastic scattering background remained. Recrystallized Bi films showed melting behaviors similar to that observed for as-deposited films, but shifted toward higher temperatures. This is due to the shift of the size distribution towards higher sizes as the crystallites recrystallized after melting.

RHEED gives a statistical view of the atomic order over a large area within a penetration depth given by the IMFP of RHEED electrons in Bi. Thus, one would use the melting range over which the phase transition occurs to study the melting behavior of the crystallites making up the films. After taking into consideration the reduction in RHEED intensity due to the Debye-Waller factor and inelastic scattering, the intensity decrease of the (220) spot of Bi is related to the fraction of the solid crystallites that are melted within the penetrated depth of the probed area. Following a procedure reported elsewhere,³⁸ the film-melted ratio R is calculated for as-deposited and recrystallized Bi crystallites and plotted in Fig. 6 as a function of temperature for films with different thicknesses. Gradual changes in the melting ratio with temperature were observed. Melting of the crystallites making up the films occurred within a range of 10–20 K. All films started to melt at temperatures below T_0 , e.g., $T_0 - 50$ K for as-deposited 1.5 ML film. A 5–15 K shift in the onset of the melting, toward higher values, was observed for recrystal-

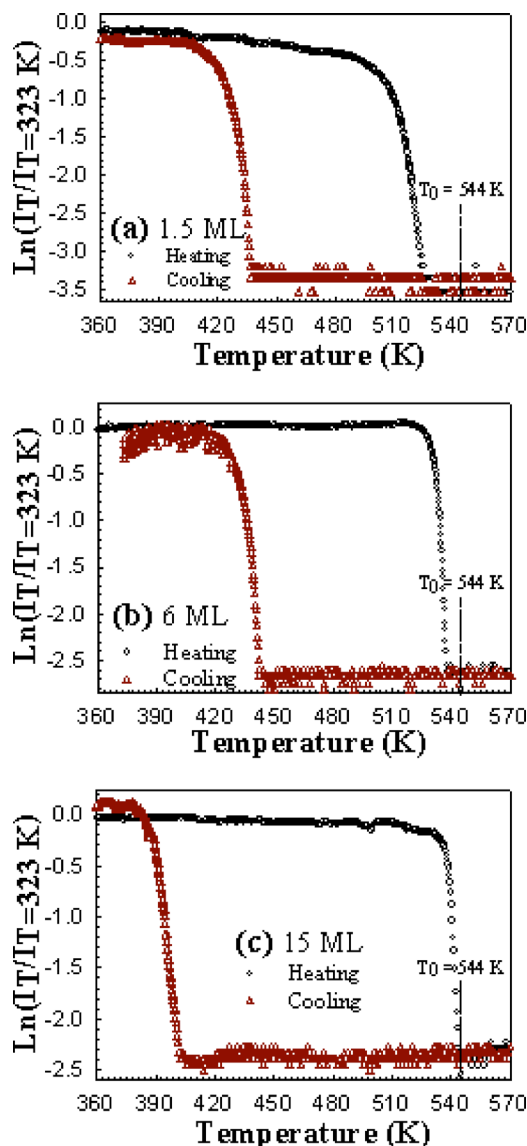


FIG. 5. Logarithm of normalized intensity of the RHEED (220) spot of Bi as a function of temperature during heating and cooling of as-deposited Bi films with different coverage. Melting point depression and supercooling that varies with the film coverage are observed.

lized Bi films of the same coverage. At the beginning of the melting temperature range, the melting ratios of as-deposited Bi films, Fig. 6(a), increased slowly with temperature. A much faster melting rate with temperature was observed as the temperature approached the film maximum melting point. This melting behavior is similar to that reported for surface melting, where the quasiliquid layer thickness grows first as a logarithmic function and then diverges as a power function of $(T - T_0)$ as T_0 is approached for bulk single crystals.³⁹ For nanocrystals, formation of a surface liquid layer is accompanied by complete melting of smaller-sized crystals.⁴⁰ The size distribution and the shape of crystallites are expected to play a major role in this melting behavior. For crystallites with similar shape, those in the lower part of the size distribution are expected to melt at a lower temperature than those in the higher part. The film-melted ratio of recrystallized Bi films, Fig. 6(b), showed a similar behavior, but the melting range was shifted toward higher tempera-

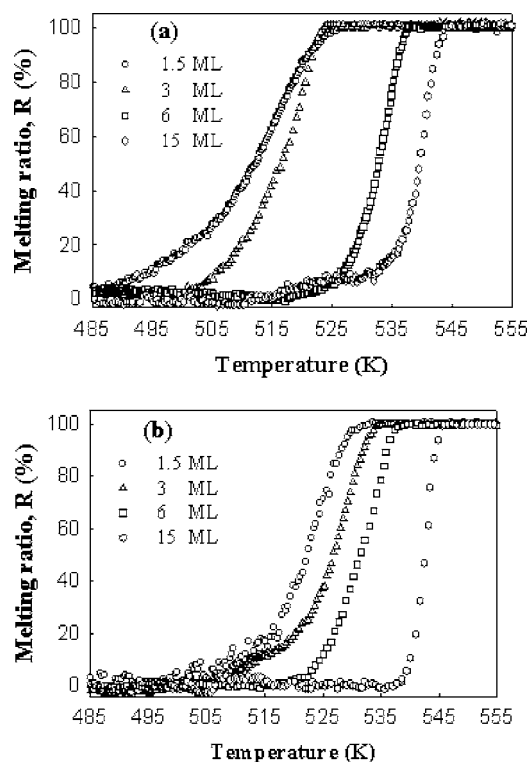


FIG. 6. Estimated film-melted ratio as a function of temperature at the phase transition region for (a) as-deposited and (b) recrystallized Bi films with different coverage.

tures. Also, for higher thickness, e.g., 15 ML, the melting occurs at a narrower melting range. This is mainly due to the shift of the size distribution towards higher values as the crystallites recrystallized after melting.

The melting behavior of the crystallites making up the films is further investigated by performing profile analysis of the obtained diffraction patterns. In general, the profile of the diffraction spots is related to the shape and size of the diffracting feature. Broadening of diffraction spots, after subtracting the instrumental response, is inversely proportional to the average crystalline size in the probed region. The probed region in this case is the shell surrounding each probed nanocrystal with ~ 9 nm thickness. The instrumental response was obtained by deflecting the electron beam away from the sample so that it directly hits the phosphor screen. The shape of the electron beam, on the phosphor screen, was recorded by the CCD camera. The FWHM of this transmitted beam, in \AA^{-1} , was used as the instrumental response and was subtracted from the FWHM of the diffraction (220) spot, obtained at different mean film thicknesses. From the broadening of the (220) spot, a diffraction feature size of ~ 4 – 7 nm is obtained, which is much less than the average nanocrystal size obtained by AFM. This is expected from a transmission RHEED pattern probing the outer shell of the nanocrystals.

Figure 7 shows the measured FWHM of the Bi (220) spot in directions parallel and normal to that of the beam for as-deposited and recrystallized Bi films with different mean thicknesses as a function of temperature. The FWHM remains almost constant over a wide temperature range in both the parallel and normal directions. However, in the film melt-

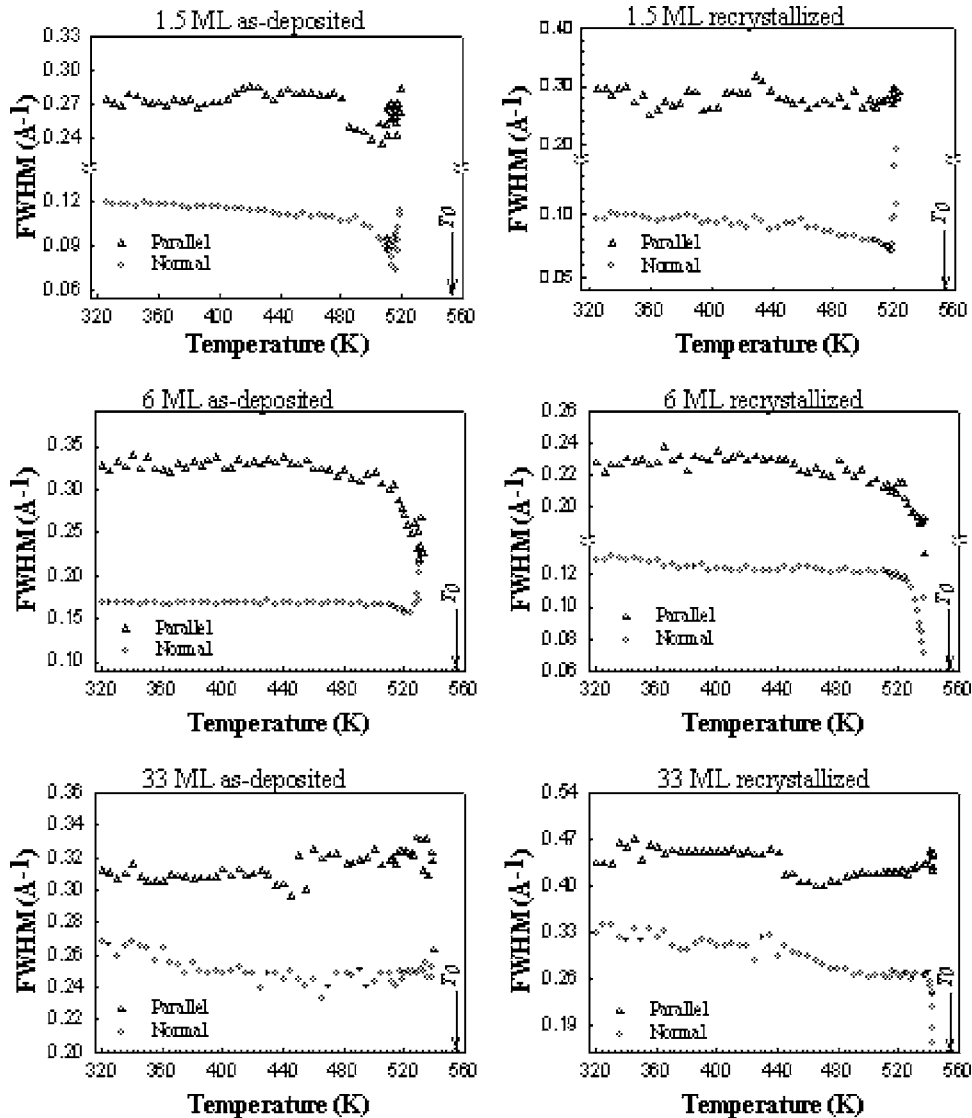


FIG. 7. The FWHM of the RHEED (220) spot for as-deposited and recrystallized Bi films with different coverage as a function of temperature in directions parallel and normal to the beam direction. The instrumental response, which is measured to be ~ 0.12 and $\sim 0.17 \text{ \AA}^{-1}$ for the parallel and normal directions, respectively, is subtracted from the plotted values.

ing range, the FWHM in both directions decreases with temperature, and then starts to increase as the maximum melting point of the film is approached. This behavior is observed for as-deposited and recrystallized 1.5 ML Bi films. The initial decrease in FWHM of the (220) spot in both directions indicates that there is an increase in the average crystalline size within the penetrated depth of the probed area. This average size increase might be due to coalescence of Bi crystallites near melting, Ostwald ripening, and/or crystal shape modification as observed in the AFM of Fig. 4. However, these effects do not explain the observed decrease in the FWHM of recrystallized films, where no further significant shape and size changes are expected. Also, no increase in the normalized intensity is observed anywhere within the film melting range, which indicates that there is no significant enhancement of the crystalline size during heating. The size increase between as-deposited and recrystallized Bi crystallites as observed by AFM can only occur by coalescence of liquid droplets after film melting. Thus, it appears that crystallites with small sizes are homogeneously melted at lower temperatures resulting in an average size increase. The observed increase in the FWHM at the end of the film melting range indicates a decrease in the detected average crystal size. This

decrease is consistent with the formation of a liquid or liquidlike shell covering the larger nanocrystals, thus, reducing the detected average crystalline size of the probed area of the films. This shell not only includes those atoms that are in the true liquid phase, where they have random structure and irregular motion, but also those having large vibrational amplitude accompanied by a few detached atoms and vacancies.⁴¹

All films with average thickness up to 15 ML showed FWHM trends similar to that observed for 1.5 ML films. Recrystallized films showed a decrease in the FWHM followed by a significant increase at a temperature close to the end of the film melting range for both the normal and parallel directions of the spot profile. AFM images of these films showed nearly polyhedral-shaped crystallites with size distributions shifted toward higher values. The average crystal size of recrystallized 1.5, 3, 6, and 15 ML films were found to be 40, 57, 83, and 100 nm, respectively. Also, as the coverage was increased, the size distribution widened. The crystallites at the lower part of the distribution are expected to melt homogeneously at a temperature in the lower part of the melting range. As the temperature is further raised into the melting range, a subset of the larger crystallites become cov-

ered by a liquid skin layer. Because of the size-dependent liquid skin formation, the liquid layer is formed on the surfaces of larger crystallites at higher temperatures relative to those with smaller sizes. With the increase in temperature, more crystallites completely melt, while the thickness of the liquid shell on the remaining crystals continues to grow with no detected reduction in the average probed size. This could be due to the shadowing effects on RHEED, where it does not probe the smaller crystallites.

The FWHM profile of the as-deposited 33 ML film remained unchanged, up to complete melting of the film, in both parallel and normal directions, while that of the recrystallized film decreased with temperature with only a small increase observed near the end of the film melting range. This observation shows the effect of crystal shape and size distribution on the melting behavior of the nanocrystals. While the as-deposited film has crystallites with different shapes, recrystallized Bi crystallites have rounded shapes and higher average sizes than the as-deposited film. Thus, melting of as-deposited films proceeded via simultaneous melting of small crystals and formation of a liquid layer on top of the larger ones, with no detectable change in the FWHM. On the other hand, the more rounded crystallites of the recrystallized film melted according to their sizes with a continuous decrease in the measured FWHM.

Within the investigated thickness range, all films melted completely below or at T_0 of Bi. AFM images showed that as-deposited films contain crystallites of round, triangular, and platelet shapes. Some of these crystal shapes are similar to that of Bi and Pb crystallites reported previously to superheat above T_0 .^{18,22} No subset of our Bi crystallites could be superheated. For rounded polyhedral Bi nanocrystals, the observed melting point depression was found to be similar to that previously reported using dark field electron microscopy.¹⁸ Elongated Bi crystallites in the as-deposited films melted at temperatures lower than that for the recrystallized round nanocrystals, however, polyhedral-shaped crystallites faceted by $\{111\}$ planes superheated up to $T_0 + 7$ K.¹⁸ These crystallites were formed during heating of Bi films initially deposited at room temperature on an amorphous carbon substrate. In the present study, polyhedral elongated crystallites were formed on a heated HOPG substrate. The shape of these crystallites was affected by the substrate and Bi grew along directions of minimum lattice mismatch and angle distortion on the HOPG basal plane. AFM images showed that these crystallites are formed in an elongated hexagonal shape of $\sim 120^\circ$ side angles ($\sim 60^\circ$ for the triangular shape) and are not in the truncated pyramidal shape. With the top surfaces of these crystallites to be $\{110\}$, as observed by RHEED, side facets could be $\{110\}$, which are $\sim 92^\circ$ with respect to the top plane as confirmed by AFM images in Fig. 4. Thus, the elongated platelet crystallites on the HOPG are not of minimum energy shapes that are completely covered by the $\{111\}$ facets; however, they are dominantly bounded by $\{110\}$ surfaces. The absence of long-range order in the amorphous carbon substrate used in Ref. 18 appears to have allowed the formation of a subset of Bi crystallites in an elongated shape with minimum energy facets that hinder surface melting and allow superheating. On the

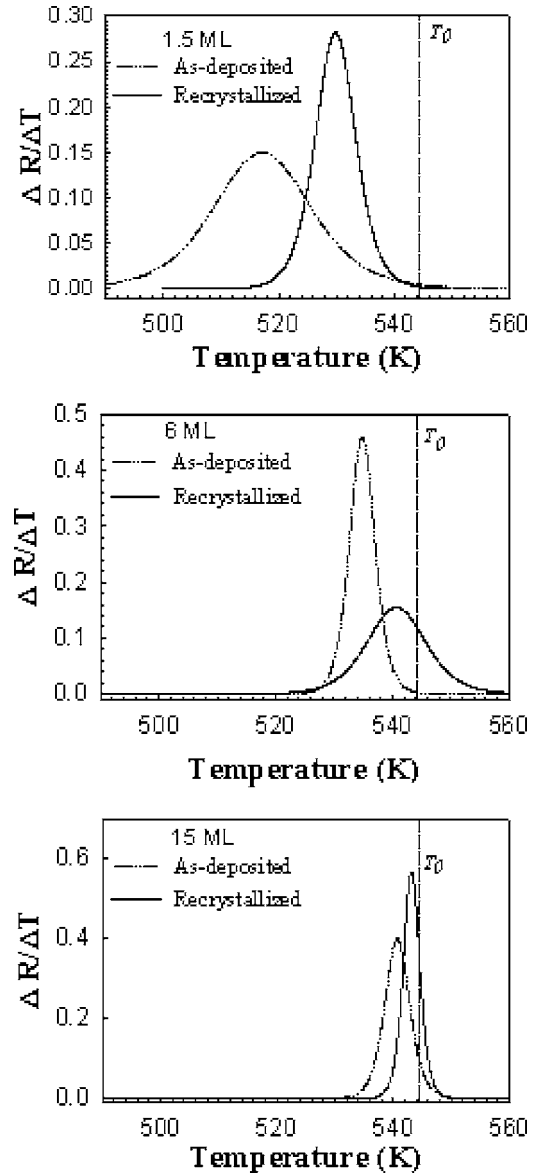


FIG. 8. Derivative of the curve fit to the melted ratio curve in Fig. 6 obtained as a function of temperature for as-deposited and recrystallized Bi films with different mean thicknesses. The peak of this derivative gives the temperature at which the rate of film melting with temperature is the fastest, T_{im} .

other hand, the long-range order of the HOPG substrate influences the formation of elongated crystallites that are dominantly bounded by $\{110\}$ facets that permit surface melting. Melt can also nucleate from curved edges where higher energy facets can exist. Using transmission electron microscopy, only Pb crystallites of triangular shape with sharp edges were reported to show 2–4 K superheating.²² Those with curved edges melted below the bulk melting point. The triangular crystallites observed in this work were of curved edges, which is consistent with the observed melting point depression.

C. Melting point-size dependence

To characterize film melting with temperature, a curve fit is made to the melted ratio data in Fig. 6 and the derivative of this curve fit is plotted in Fig. 8 for the as-deposited and

recrystallized films. The peak of this derivative gives the temperature at which the rate of film melting with temperature increase is the fastest, T_{fm} . We use T_{fm} to represent the characteristic film melting temperature, with a range that we define to correspond to 10% and 90% of the melted ratio in Fig. 6. Melting point depression that depends on the film coverage is clearly observed in Fig. 8. Also, recrystallized films showed higher T_{fm} than as-deposited films for all thicknesses. This is mainly due to the average size increase. From the AFM images of as-deposited and recrystallized films, we calculated a shape-independent average crystal radius, $r_{av} = [(3 \times \text{area} \times \text{height}) / (4\pi)]^{1/3}$, by measuring the area and the height of the nanocrystals from AFM images. The values of T_{fm} obtained for as-deposited films were lower than that obtained for recrystallized films with equal thickness for all films. This is consistent with the average crystal size increase as the films recrystallized after melting, causing the recrystallized films to have a higher T_{fm} .

We used the values of T_{fm} and r_{av} to compare the melting point-size dependence of Bi films with different phenomenological models. The use of r_{av} as a representative radius is made since all models considered a spherical particle. There are many phenomenological models describing the melting point-size dependence of nanometer-sized crystals.^{7-10,42-44} All of them predicted a linear or semilinear relation between the melting point of the crystals and the reciprocal of its radius. These models can be summarized as the homogeneous melting (HM) model,^{8,9} liquid skin (LS) model,⁷⁻¹⁰ the liquid-drop (LD) model,⁴² nucleation and growth (NG) model,⁴³ surface-phonon instability (SPI) model,⁴⁴ and the lattice vibration-based (LV) model.⁴⁵ In the HM model, the melting point is the point at which the melt and the solid coexist homogeneously in equilibrium. According to this model, the size dependence of the melting point is described by,^{8,9}

$$T_m = T_0 - \frac{2T_0}{\rho_s L r} \left[\gamma_{sv} - \gamma_{lv} \left(\frac{\rho_s}{\rho_l} \right)^{2/3} \right], \quad (1)$$

where T_0 is the bulk melting point, T_m is the melting point of a particle of radius r , L is the latent heat of fusion, γ and ρ are the surface energy per unit area and the density of the phase, and the subscripts s , l , and v are used to refer to solid, liquid, and vapor phases, respectively. The LS model considers a core of solid particles covered with its liquid melt. The melting point of this nanocrystal is then defined as the point where the core is in equilibrium with the liquid skin at its critical thickness. The relation between the melting point and the crystal size is found to be⁷⁻¹⁰

$$T_m = T_0 - \frac{2T_0}{\rho_s L} \left[\frac{\gamma_{sl}}{(r - \delta)} + \frac{\gamma_{lv}}{r} \left(1 - \frac{\rho_s}{\rho_l} \right) \right], \quad (2)$$

where δ is an adjustable critical liquid thickness. In the NG model, melting starts by the nucleation of a liquid layer at the surface and moves into the solid with definite activation energy. The temperature range where the solid and liquid can coexist in equilibrium, and hence the liquid can grow, is defined to be^{10,43}

$$T_m = T_0 - \frac{2T_0}{Lr} \alpha_{NG} \quad \text{where } \gamma_{sl} < \alpha_{NG} < \frac{3}{2} \left(\gamma_{sv} - \gamma_{lv} \frac{\rho_s}{\rho_l} \right). \quad (3)$$

Outside this range, only a single phase, either solid or liquid, can exist. In the LD model, an empirical relation between the cohesive energy, surface tension, and the melting temperature is used, in analogy to the liquid-drop model used in describing the nucleus structure. An expression for the size-dependent melting for low-dimensional systems is derived such that⁴²

$$T_m = T_0 \left(1 - \frac{\beta}{r} \right), \quad (4)$$

where β is a surface energy dependent constant given for Bi to be equal to 2.1273 nm.⁴² The SPI model assumes that the mean phonon frequency of the particles varies linearly with the number of defects and surface sites produced in the nanoparticle.⁴⁴ A relation between the particle melting point and its radius is found to have a form similar to that of Eq. (4). However, in this case, the constant β is varied depending on the bulk melting temperature and the energy of formation of intrinsic defects. For Bi, this constant is found to be equal to 0.86 nm.⁴⁴ The LV model is another approach that does not include any adjustable parameter.⁴⁵ It is based on Lindemann's criterion and Mott's expression of the vibrational entropy. A melting point-size dependence is formulated such that⁴⁴

$$T_m = T_0 \exp \left[\frac{-(2S_{vib}/3R)}{(r/6h) - 1} \right], \quad (5)$$

where S_{vib} is the vibration entropy of melting of the bulk crystal, h is the atomic diameter, and R is the ideal gas constant. The known physical constants of Bi ($T_0 = 544.52$ K, $\rho_s = 9.8$ g/cm³, $\rho_l = 10.07$ g/cm³, $L = 5.19 \times 10^{-8}$ erg/g, $\gamma_{sl} = 61$ erg/cm², $\gamma_{sv} = 550$ erg/cm², $\gamma_{lv} = 375$ erg/cm², $h = 0.4074$ nm, $S_{vib} = 3.78$ J mole⁻¹ K⁻¹, and $R = 8.3142$ J mole⁻¹ K⁻¹) were used to calculate the melting point-size dependence of Bi.^{7,17,43,44} Figure 9 shows the size-dependent behavior predicted by these models compared to the results obtained from the present work. In calculating the melting point using the NG model, we used the average value of the parameter α_{NG} . Also, we used an arbitrary value of $\delta = 4$ nm in the calculation using the LS model. However, varying this value between 2 and 10 nm does not affect the obtained results for particles of radius within the current experimental values; it only affects the melting point of particles with radius close to the value of δ .

The size-dependent phenomenological models have two characteristics in common: T_m converges to T_0 as the radius goes to infinity, and a linear or semilinear relation exist between T_m and r^{-1} of the particle. Straight lines with different slopes are obtained for Bi using these models, with LV and HM models showing strong agreement with each other. The melting points calculated by these models converge to T_0 for the larger sizes. Considering the range of crystallite sizes we studied, the melting data show best agreement with the SPI model. This means that the loss of long-range order in the

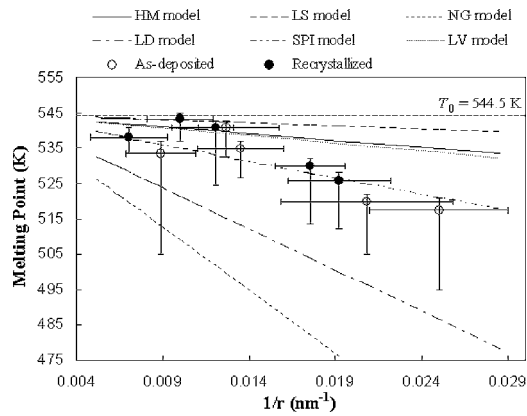


FIG. 9. The measured characteristic melting point of T_{fm} as a function of the reciprocal of the average crystalline size compared to different thermodynamic models. T_{fm} is obtained from Fig. 8. The vertical bars represent the melting range as described in the text, while the horizontal bars represent the error in the measured r^{-1} , $\Delta(r^{-1}) = \Delta r / r^2$ and Δr is the standard deviation. The surface-phonon instability (SPI) model agrees best with the experimental results.

top layers and liquid layer formation detected by RHEED are described best using a single-phase microscopic view, rather than a two-phase macroscopic view. Thus, the atoms are dislodged from their equilibrium positions and a disordered liquid layer is formed via proliferation of intrinsic defects within the top layers. On the other hand, using a macroscopic description of a liquid layer in equilibrium with a solid core is not consistent with the current data for Bi nanocrystals. In Fig. 9, the open circles represent data obtained for as-deposited crystallites, while the solid circles are for the recrystallized ones. No distinction in melting point dependence on r is observed. Thus, for the studied conditions, the shape of the crystallites had an insignificant effect on the melting behavior.

D. Film solidification

During solidification, the Bi films showed high amount of supercooling relative to the onset of its melting and to T_0 of bulk Bi. A wide melting-solidification hysteresis curve that varied with the film average thickness was observed for as-deposited Bi films as shown in Fig. 5. In general, super-

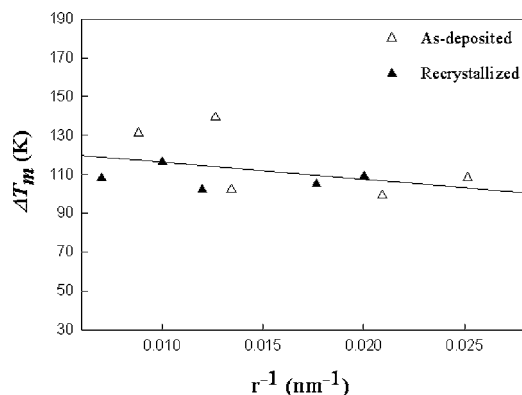


FIG. 10. The measured amount of supercooling as a function of the reciprocal of the average crystallite size. A straight line with a negative slope best fits the results, consistent with Eq. (6).

cooling is attributed to the presence of a nucleation barrier for solidification that results from the competition between the decrease in the volume free energy upon solidification and the increase in the free energy associated with the existence of a solid-liquid interface. Classical nucleation theory predicts that solidification occurs with a lower energy barrier on heterogenous sites than homogeneously from within the liquid. The energy barrier for solidification decreases as the liquid is supercooled below its bulk melting point. Furthermore, if the liquid is deeply supercooled, spontaneous solidification can occur with zero energy barriers. For a bulk liquid, this occurs after a supercooling amount of ΔT_0 . However, for a small droplet, spontaneous solidification starts at a different temperature given by¹⁵

$$\Delta T_m = \Delta T_0 + \frac{T_0}{\rho L} \frac{3\alpha\Delta\gamma}{r}, \quad (6)$$

where ΔT_m is the amount of supercooling of a melted particle of radius r , α is the fraction of the liquid/substrate interface that is replaced by the solid/substrate interface after solid nucleation, and $\Delta\gamma = \gamma_{\text{solid/graphite}} - \gamma_{\text{liquid/graphite}}$, where $\gamma_{\text{solid/graphite}}$ and $\gamma_{\text{liquid/graphite}}$ are the specific interfacial energies between the graphite substrate and the solid and liquid Bi, respectively. The amount of supercooling obtained from as-deposited and recrystallized films is plotted as a function of the calculated shape-independent average crystal size as shown in Fig. 10. The obtained supercooling amount ΔT_m fits a straight line with a small negative slope for as-deposited as well as recrystallized Bi crystallites. This indicates a supercooling amount increase as the droplet size increases. From Eq. (6), the sign of the slope of the straight line is determined by the sign of $\Delta\gamma$. In our case, $\Delta\gamma$ is negative, consistent with a liquid Bi that has a higher interfacial energy with the graphite substrate than its solid phase. Accordingly, crystallites with larger sizes have a higher supercooling amount. The maximum supercooling is for the bulk material, which is found from the curve intercept with the y axis to be $\Delta T_0 = 126$ K.

IV. SUMMARY AND CONCLUSIONS

Bi films with average thicknesses of 1.5–33 ML thermally deposited on a heated HOPG were studied using *in situ* RHEED and AFM. RHEED patterns of Bi films, performed at room temperature, showed transmission patterns of the rhombohedral structure of Bi showing textured and/or multioriented nanocrystals. Postdeposition AFM showed that both as-deposited and recrystallized films were composed of separate 3D crystallites with different sizes. Crystallites with different shapes including rounded, polyhedral, elongated platelet, and triangular shapes were observed in as-deposited films. Recrystallized crystallites were formed in faceted and/or rounded polyhedral similar shapes. The elongated crystallites were found to align themselves in the directions of minimum lattice misfit and angular distortion on the 002-graphite plane. The crystallites were uniformly distributed throughout the substrate surface except at terrace edges where a higher density of crystallites was found. The distri-

butions became wider and shifted toward higher values as the thickness was increased.

With heating, the Bi films showed a gradual solid-liquid phase transition. Melting of the crystallites making up the films occurred at temperatures lower than T_0 and spanned over a temperature range whose onset and end points increased with the film coverage. Due to size increase after melting, the recrystallized crystallites showed a melting range at temperatures higher than that of the as-deposited crystallites. Within the investigated thickness range, all the nanocrystal shapes showed size-dependent melting point depression, and the films were melted completely below or at T_0 of Bi. Formation of the elongated platelet crystals due to an epitaxial-like growth mode, rather than minimum energy shape, explains its observed melting point depression. RHEED profile analyses showed that small crystallites melt first, while liquid skin formation on the curved surfaces of larger crystallites continues to grow in thickness causing a size-dependent melting. The characteristic film melting point of Bi showed a linear dependence on the reciprocal of the average crystal radius, in agreement with different phenomenological theoretical models. The surface-phonon instability model best fits our data.

During solidification, as-deposited and recrystallized Bi crystallites showed large supercooling relative to T_0 . The amount of liquid supercooling was found to decrease linearly with the reciprocal of the average crystal size.

ACKNOWLEDGMENTS

This material is based upon work supported by the National Science Foundation under Grant No. DMR-9988669 and by the US Department of Energy, Division of Material Sciences, under Grant No. DE-FG02-97ER45625.

¹R. S. Berry, *Microscale Thermophys. Eng.* **1**, 1 (1997).

²K. Lu and Z. H. Jin, *Curr. Opin. Solid State Mater. Sci.* **5**, 39 (2001).

³Y. Qi, T. Cagin, W. L. Johnson, and W. A. Goddard III, *J. Chem. Phys.* **115**, 385 (2001).

⁴M. L. Lavčević and Z. Ogorelec, *Mater. Lett.* **57**, 4134 (2003).

⁵L. J. Lewis, P. Jensen, and J. Barrat, *Phys. Rev. B* **56**, 2248 (1997).

⁶F. Ercolessi, W. Andreoni, and E. Tosatti, *Phys. Rev. Lett.* **66**, 911 (1991).

⁷G. L. Allen, R. A. Bayless, W. W. Gile, and W. A. Jesser, *Thin Solid Films* **144**, 297 (1986).

⁸Ph. Buffat and J. P. Borel, *Phys. Rev. A* **13**, 2287 (1976).

⁹T. Castro, R. Reifenberger, E. Choi, and R. P. Andres, *Phys. Rev. B* **42**,

8548 (1990).

¹⁰M. Zhang *et al.*, *Phys. Rev. B* **62**, 10548 (2000).

¹¹L. Zhang, Z. H. Jin, L. H. Zhang, M. L. Sui, and K. Lu, *Phys. Rev. Lett.* **85**, 1484 (2000).

¹²N. T. Gladkikh, S. I. Bogatyrenko, A. P. Kryshnal, and R. Anton, *Appl. Surf. Sci.* **219**, 338 (2003).

¹³N. B. Thofit, J. Bohrf, B. Burast, E. Johnsons, A. Johansens, H. H. Andersens, and L. Sarholt-Kristensens, *J. Phys. D* **28**, 539 (1995).

¹⁴H. H. Andersen and E. Johnson, *Nucl. Instrum. Methods Phys. Res. B* **106**, 480 (1995).

¹⁵H. W. Sheng, K. Lu, and E. Ma, *Acta Mater.* **46**, 5195 (1998).

¹⁶J. D. Mackenzie and R. L. Cormia, *J. Chem. Phys.* **39**, 250 (1963).

¹⁷J. F. van der Veen, B. Pluis, and A. W. D. van der Gon, in *Chemistry and Physics of Solid Surfaces VII* (Springer-Verlag, Berlin, 1988), pp.455–490.

¹⁸S. J. Peppiatt, *Proc. R. Soc. London, Ser. A* **345**, 401 (1975).

¹⁹M. Blackman, S. J. Peppiatt, and J. R. Samples, *Nature (London), Phys. Sci.* **239**, 61 (1972).

²⁰V. P. Skripov, V. P. Koverda, and V. N. Skokov, *Phys. Status Solidi A* **66**, 109 (1981).

²¹M. Takagi, *J. Phys. Soc. Jpn.* **9**, 359 (1954).

²²J. J. Mètois and J. C. Heyraud, *J. Phys. (France)* **50**, 3175 (1989).

²³G. D. T. Spiller, *Philos. Mag. A* **46**, 535 (1982).

²⁴A. A. Shvartsburg and M. F. Jerrold, *Phys. Rev. Lett.* **85**, 2530 (2000).

²⁵Z. H. Zhang, P. Kulatunga, and H. E. Elsayed-Ali, *Phys. Rev. B* **56**, 4141 (1997).

²⁶J. C. Heyraud and J. J. Mètois, *Surf. Sci.* **128**, 334 (1983).

²⁷J. C. Heyraud and J. J. Mètois, *Surf. Sci.* **177**, 213 (1986).

²⁸M. K. Zayed and H. E. Elsayed-Ali, *Thin Solid Films* **489**, 42 (2005).

²⁹M. K. Zayed and H. E. Elsayed-Ali, *Phys. Rev. B* **72**, 205426 (2005).

³⁰J. C. Patrin, Y. Z. Li, M. Chander, and J. W. Weaver, *Phys. Rev. B* **46**, 10221 (1992).

³¹M. Mašek and V. Matolín, *Vacuum* **61**, 217 (2001).

³²S. Andrieu and P. Frechard, *Surf. Sci.* **360**, 289 (1996).

³³K. Mae, V. V. Moshchalkov, and Y. Bruynseraede, *Thin Solid Films* **340**, 145 (1999).

³⁴C. J. Powell, A. Jablonski, I. S. Tilinin, S. Tanuma, and D. R. Penn, *J. Electron Spectrosc. Relat. Phenom.* **98&99**, 1 (1999).

³⁵Z. Wang and P. Wynblatt, *Surf. Sci.* **398**, 259 (1998).

³⁶J. C. Patrin, Y. Z. Li, M. Chander, and J. H. Weaver, *J. Vac. Sci. Technol. A* **11**, 2078 (1993).

³⁷H. Wang, J. Jing, and P. N. Henriksen, *J. Vac. Sci. Technol. A* **11**, 1987 (1993).

³⁸M. K. Zayed, M. S. Hegazy, and H. E. Elsayed-Ali, *Thin Solid Films* **449**, 254 (2004).

³⁹B. Pluis, T. N. Taylor, D. Frenkel, and J. F. Van der Veen, *Phys. Rev. B* **40**, 1353 (1998).

⁴⁰K. F. Peters, Y.-W. Chung, and J. B. Cohen, *Appl. Phys. Lett.* **71**, 2391 (1997).

⁴¹H.-P. Cheng and R. S. Berry, *Phys. Rev. A* **45**, 7969 (1992).

⁴²K. K. Nanda, S. N. Sahu, and S. N. Behera, *Phys. Rev. A* **66**, 013208 (2002).

⁴³H. Reiss, P. Mirable, and R. L. Whetten, *J. Phys. Chem.* **92**, 7241 (1998).

⁴⁴M. Wautelet, *J. Phys. D* **24**, 343 (1991).

⁴⁵L. H. Liang, J. C. Li, and Q. Jiang, *Physica B* **334**, 49 (2003).